

1 **Supplemental Material to: Ice core evidence for major volcanic**
2 **eruptions at the onset of Dansgaard-Oeschger warming events**

3 Johannes Lohmann¹ and Anders Svensson¹

4 ¹*Physics of Ice, Climate and Earth, Niels Bohr Institute, University of Copenhagen, Denmark*

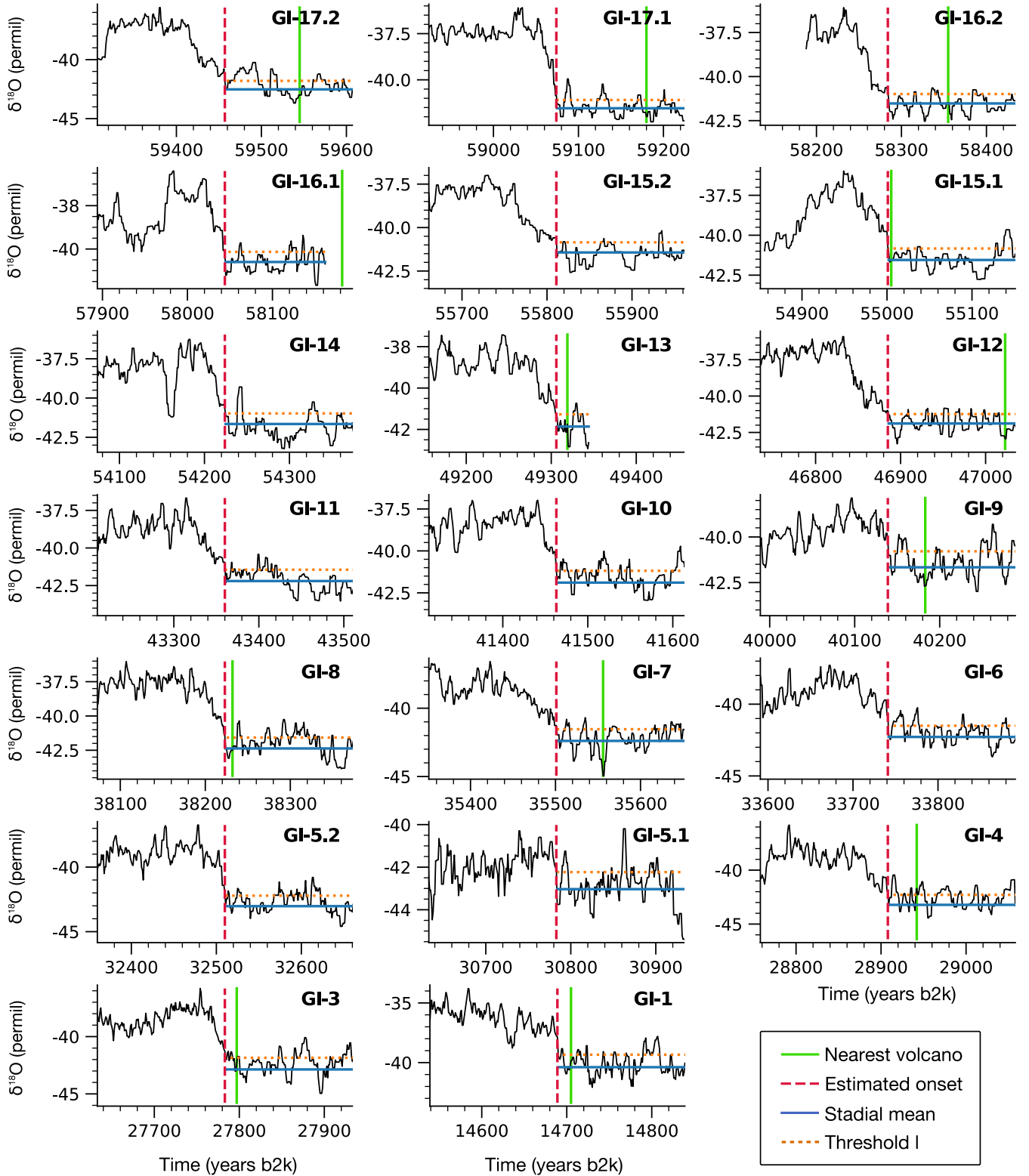


FIG. S1. Estimated onsets of the DO warming events in the Greenland $\delta^{18}\text{O}$ stack and closest bipolar volcanic eruptions preceding the events. Also shown is the lower threshold l , which is used to define the transition onset with the method given in Appendix A.

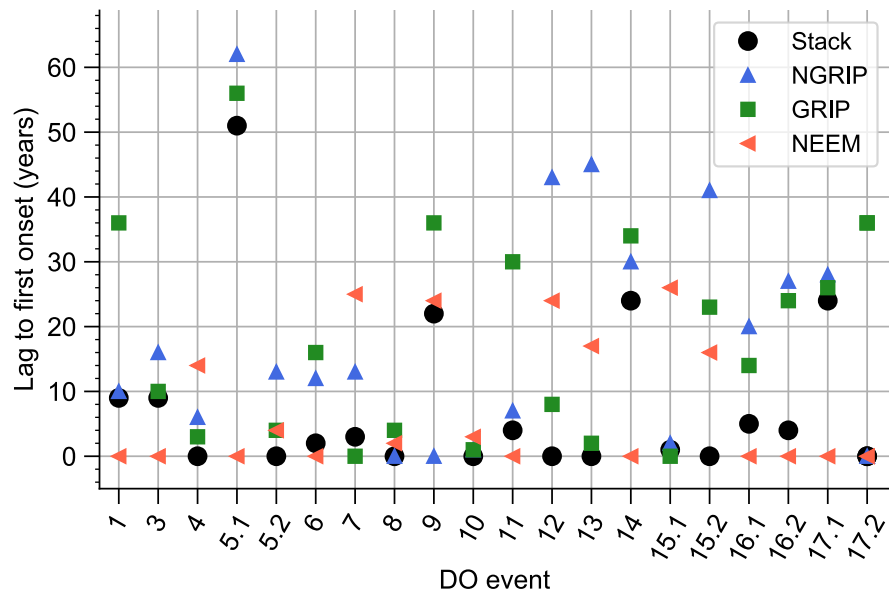


FIG. S2. DO event onsets estimated from the isotope stack and individual ice cores. Shown is the lag of individual onset estimates relative to the earliest onset estimate.

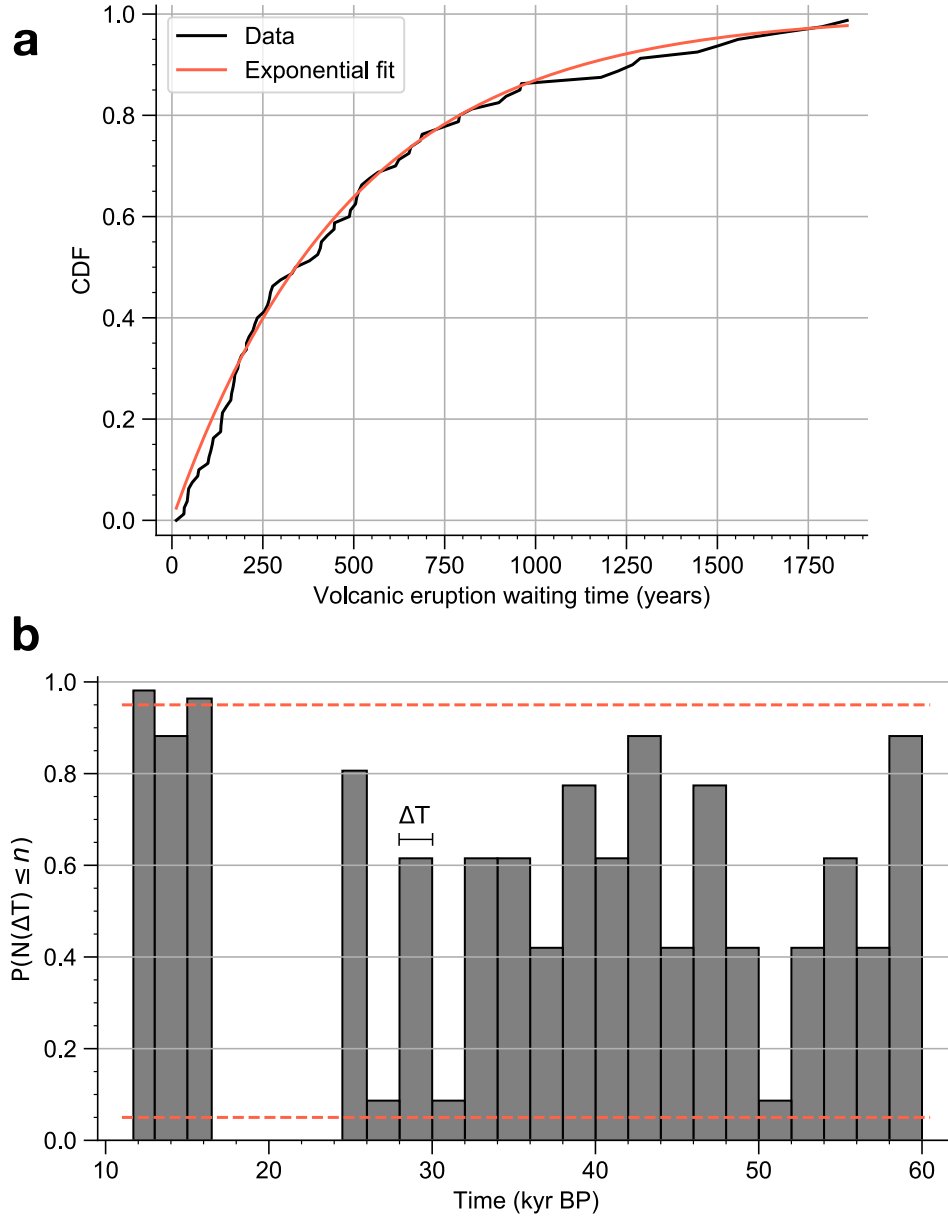


FIG. S3. a) Empirical distribution function of the bipolar volcano waiting times, compared to a fit with an exponential distribution. b) Probabilities to find less or equal than the n observed volcanic eruptions in contiguous intervals of ΔT years for a Poisson process with $\lambda = 2.0348$. The time interval ΔT has been chosen to be 2 kyr, except at the boundaries of the data. The red dashed lines indicate $P = 0.95$ and $P = 0.05$. Thus, if the data fall outside these margins, we can reject the null hypothesis at 90% confidence in a two-tailed test. However, at this confidence we expect 2.1 false positives due to the testing of 21 independent hypotheses.

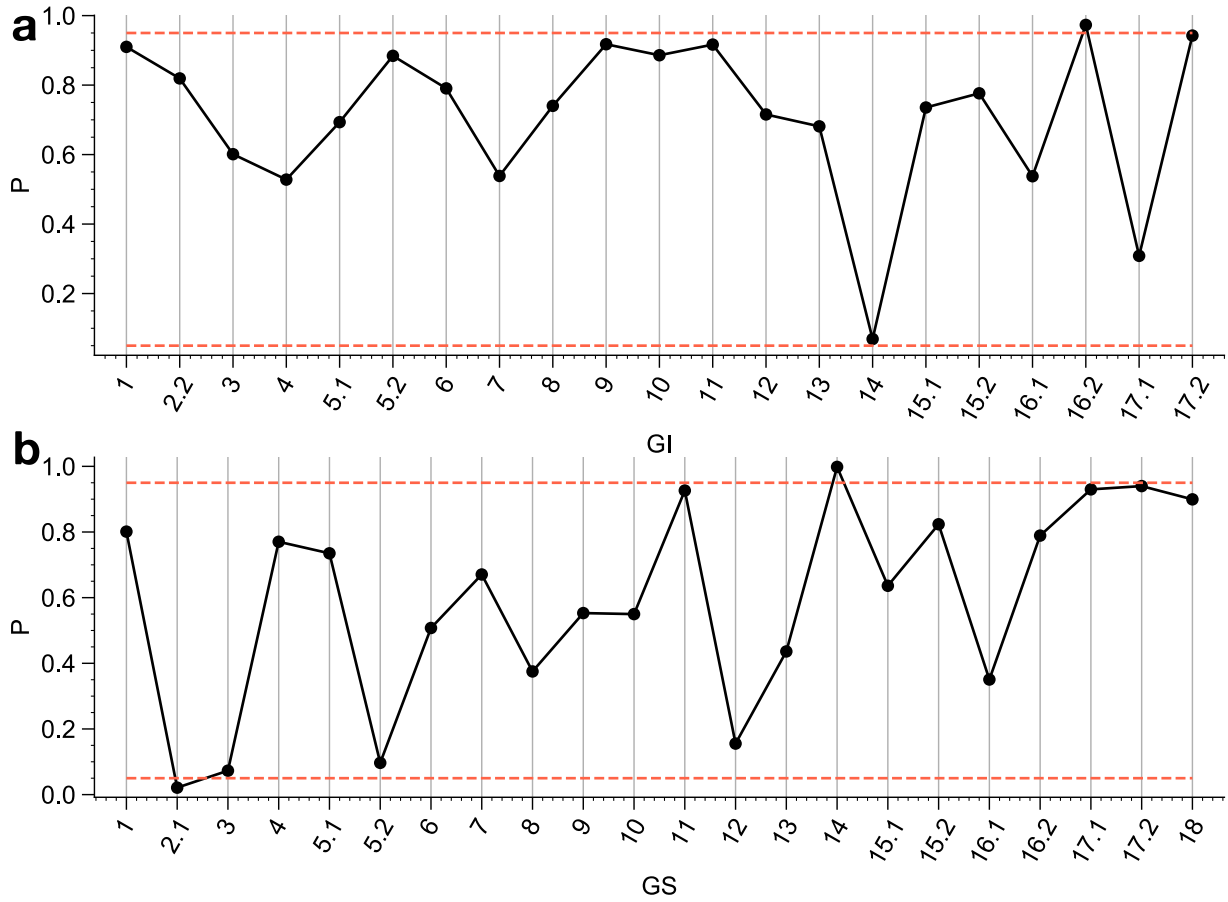


FIG. S4. Probabilities to find less or equal than the n observed volcanic eruptions in the interstadials (a) and stadials (b) for a Poisson process with $\lambda = 2.0348$. The red dashed lines indicate $P = 0.95$ and $P = 0.05$. Thus, if the data fall outside these margins, we can reject the null hypothesis at 90% confidence in a two-tailed test. However, at this confidence we expect 2.1 false positives due to the testing of 21 independent hypotheses.

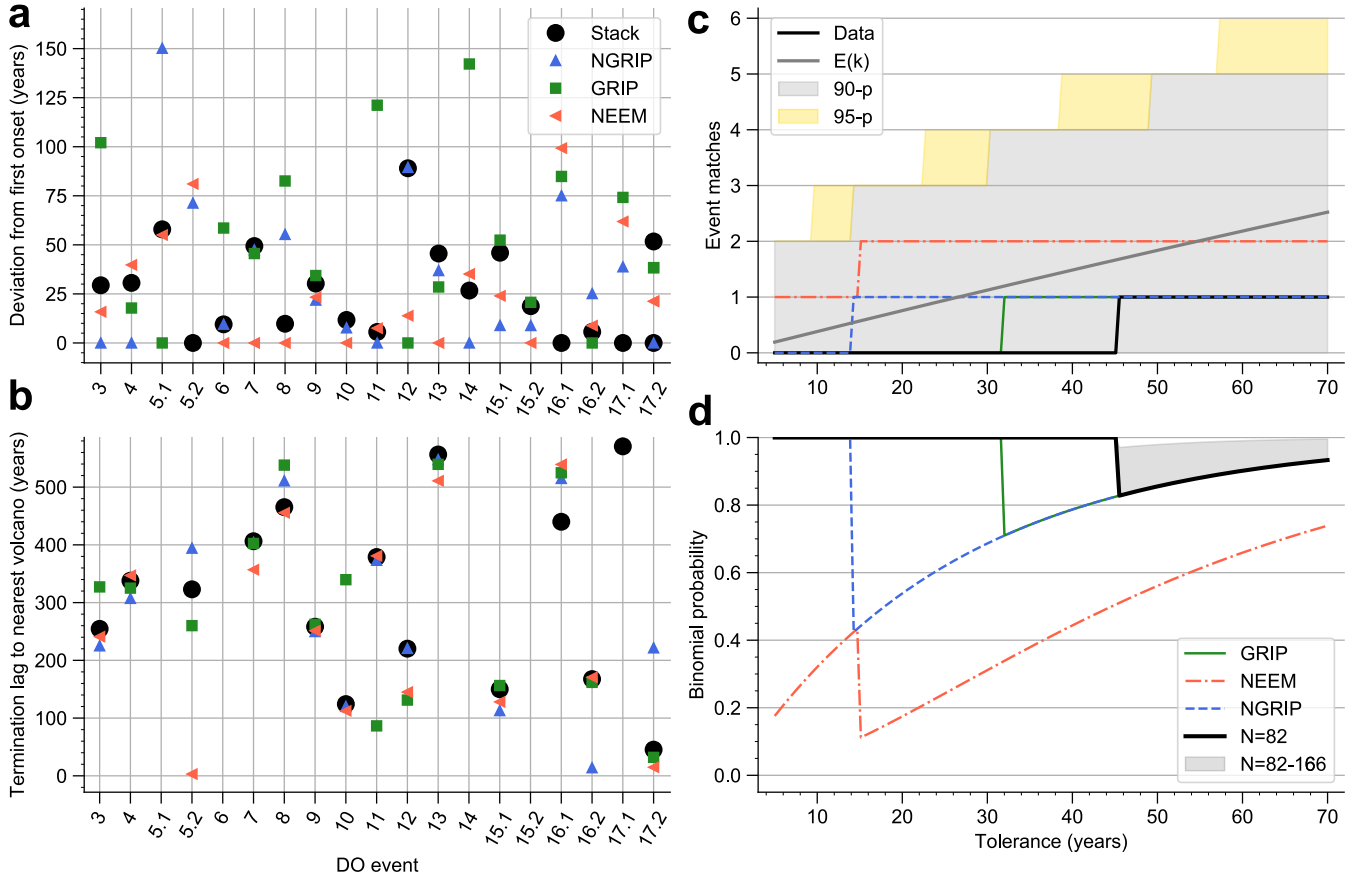


FIG. S5. Comparison of the terminations of DO interstadials with the closest preceding bipolar volcanic eruptions. a) DO interstadial terminations estimated from the stack and different ice cores using the piecewise-linear method from Lohmann and Ditlevsen, *Clim. Past* 15, 1771 (2019). Shown is the lag relative to the earliest termination. b) Lag of the individual DO terminations to the nearest volcanic eruption in the stack and different ice cores. c) Number of event matches for the terminations as a function of the tolerance, compared to the expectation value as well as 90% and 95% confidence bands of the null hypothesis. d) Probability to observe at least as many event matches as in the data under the null hypothesis. The thick black line shows the results for the stack terminations and the Poisson null hypothesis using $\lambda = N/\Delta T$ with $N = 82$. The gray shading indicates the range of probabilities when increasing N from $N = 82$ to $N = 166$. Results for the terminations from individual cores with $N = 82$ are also shown.

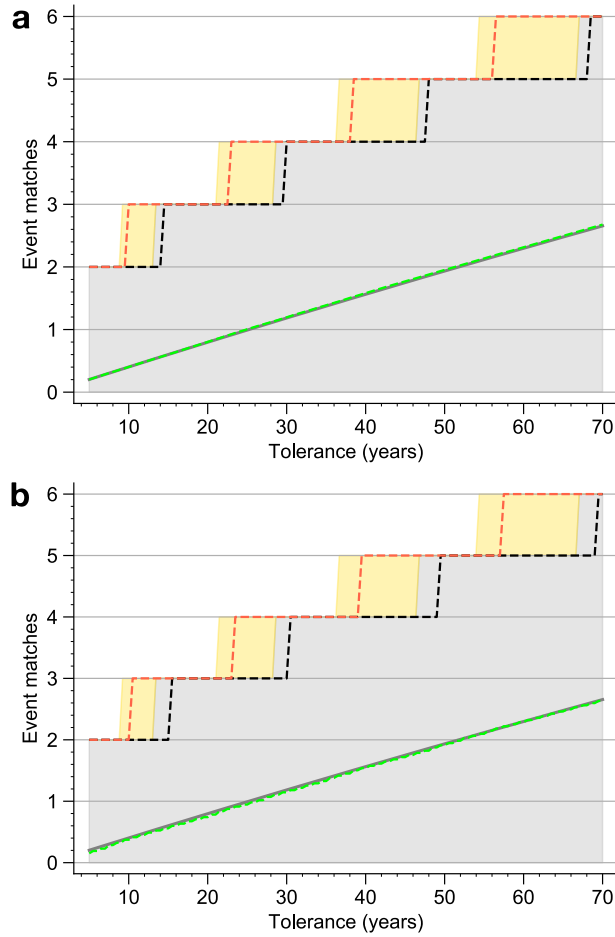


FIG. S6. Demonstration that our analytical results for the probabilities of matches under the null hypothesis closely correspond to direct Monte Carlo sampling, where the actually observed data are used without assumptions on the underlying event processes. **a** The DO onsets are fixed at their observed times, but the volcanic eruptions are sampled according to a Poisson point process on the real line with the observed rate λ . Here the real line corresponds to the time interval from 60 to 11.7 ka, while discarding eruptions in the data gap from 16.5 ka to 24.5 ka. Thereafter, the number of event matches, i.e., instances where one or more eruptions occur within a given tolerance prior to a DO onset, is recorded. This is repeated many times to calculate expectation values and percentiles. The solid gray line corresponds to the analytical expected value, and the shadings are the analytical 90- and 95-percentiles, as also seen in Fig. 5a of the main text. The dashed lines are the expectation values and percentiles of the Monte Carlo simulations. **b** In addition to the observed DO onset times, we now do not assume a Poisson process for the volcanic eruptions, but rather generate bootstrapped samples of eruptions by sampling from the observed waiting times in between eruptions with replacement.

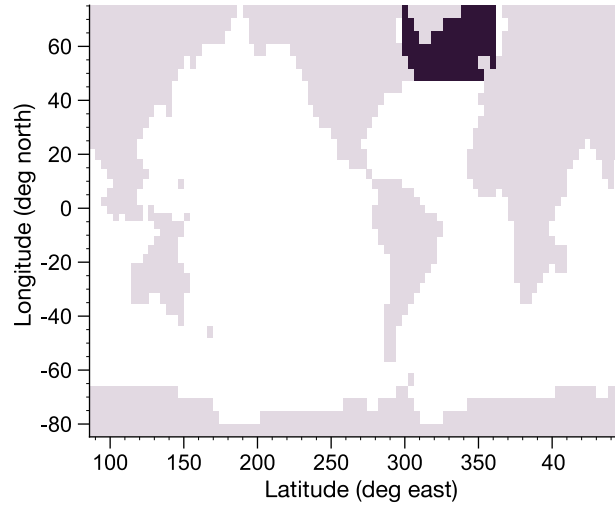


FIG. S7. Map of the model grid cells at the sea surface, where the dark cells indicate the location of the freshwater forcing anomaly in our hysteresis experiments.

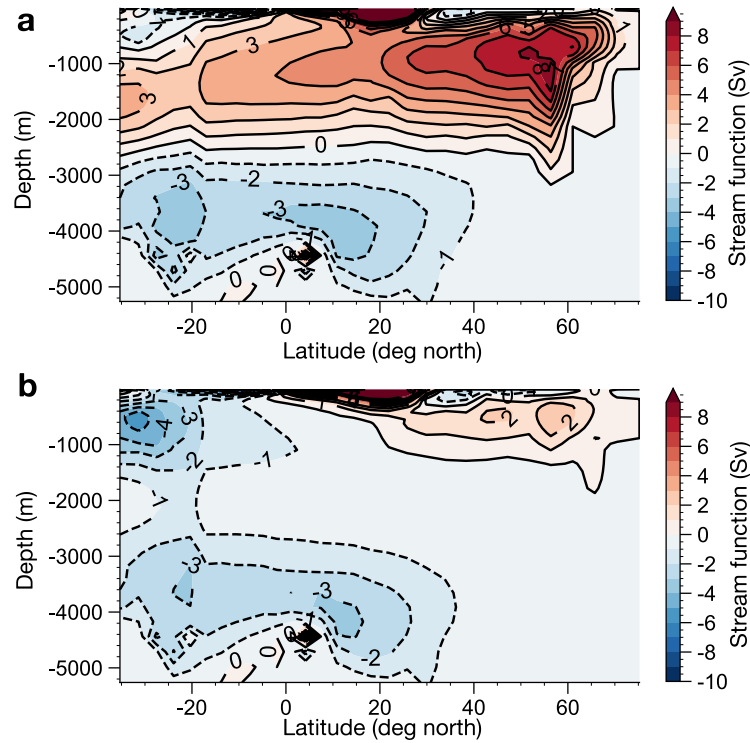


FIG. S8. AMOC stream function for simulations with a fixed freshwater forcing $F = 0.343$ Sv. The simulations were branched off from the hysteresis experiment with (a) increasing and (b) decreasing F , corresponding to the states of vigorous and (nearly) collapsed AMOC, respectively, and continued at fixed F for 20,000 years. Shown are the meridional stream functions as an average over the last 200 years of the simulations.

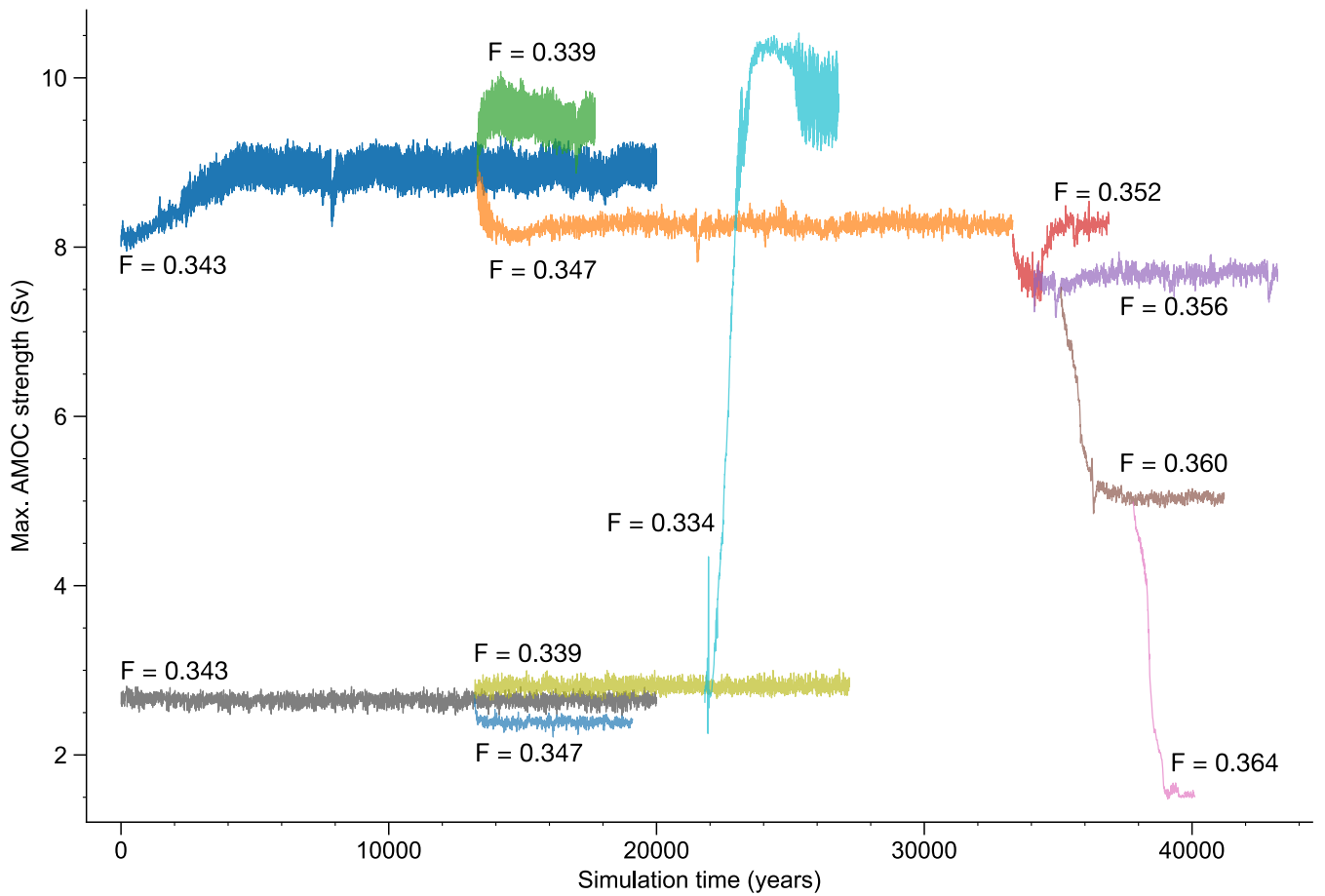


FIG. S9. 5-year moving average time series of the maximum of the NH AMOC stream function below 500 meters depth for equilibrium simulations at different values F of the freshwater forcing. The first two simulations were branched off at $F = 0.343$ from the hysteresis experiment with increasing F (dark blue), and decreasing F (gray). In the lower branch (collapsed AMOC), the circulation resurges when decreasing the freshwater forcing to $F = 0.334$. When increasing the freshwater forcing in the upper branch, the circulation partly collapses at $F = 0.360$ and then fully collapses at $F = 0.364$.

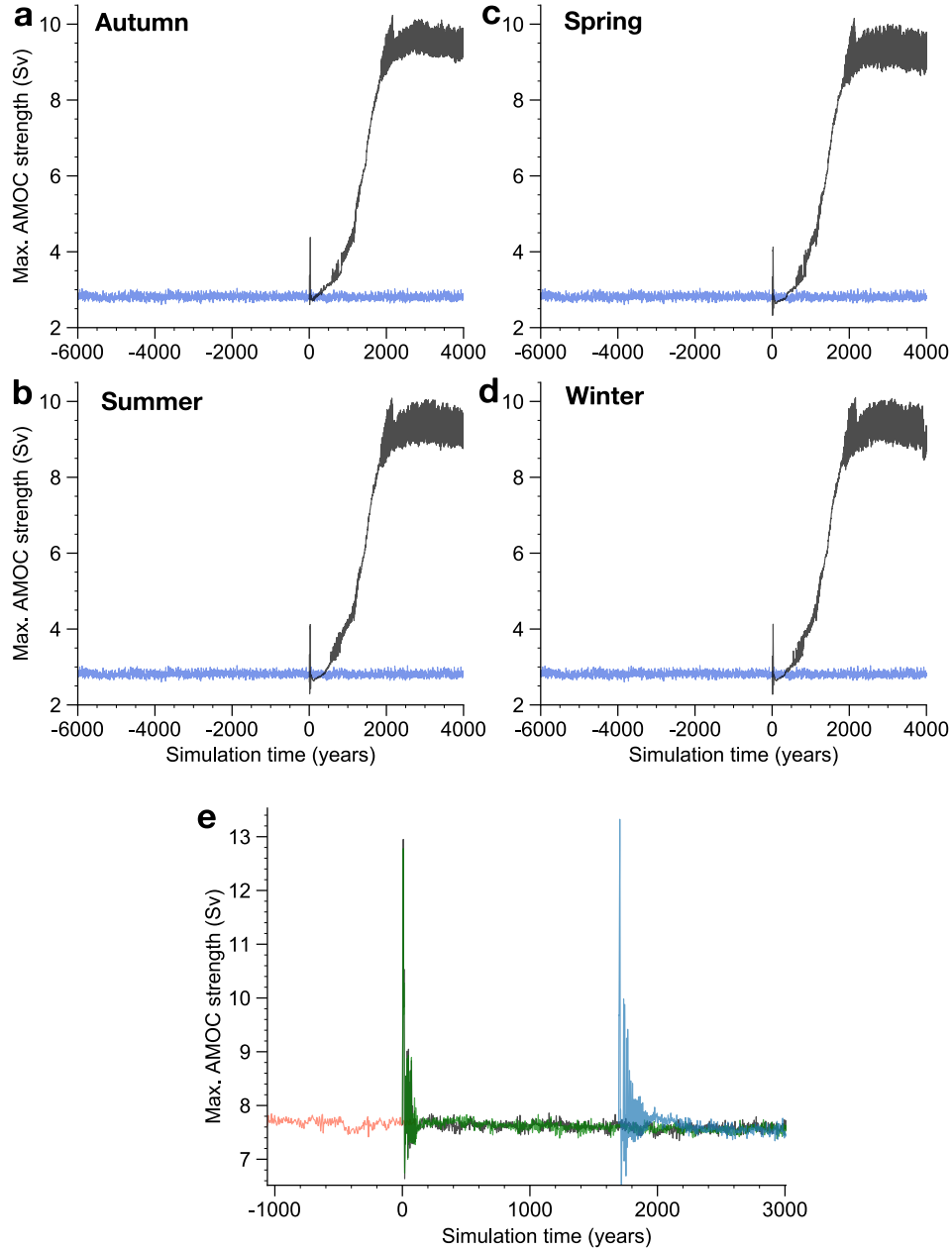


FIG. S10. **a - d** Simulations of a NH/equatorial volcanic cooling scenario (see Fig. 6c) initialized from a spinup simulation (blue) in the collapsed AMOC branch at $F = 0.339$. The different panels show simulations where the (otherwise identical) volcanic cooling signal is initiated at different times of the year. **e** Simulations of a NH/equatorial volcanic cooling scenario initialized from a spinup simulation in the vigorous AMOC branch at $F = 0.356$ (red). Realizations where the cooling is initiated in the autumn and the spring are shown in black and green, respectively. Further, a realization initiated in the autumn and with a doubled cooling magnitude compared to the scenario in Fig. 6c is shown in blue.

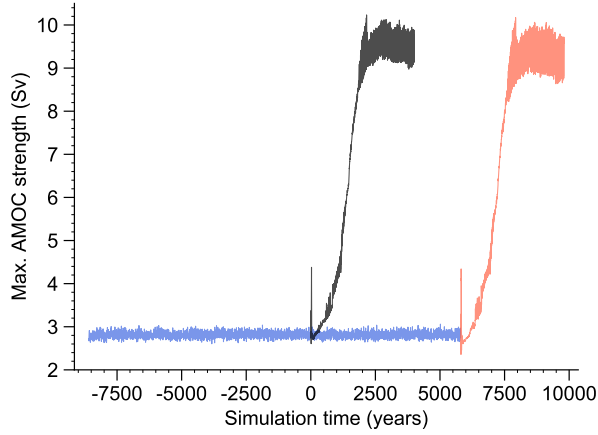


FIG. S11. Simulations of a NH/equatorial volcanic cooling scenario (see Fig. 6c) that are initialized from different initial conditions of a spinup simulation (blue) in the collapsed AMOC branch at $F = 0.339$.

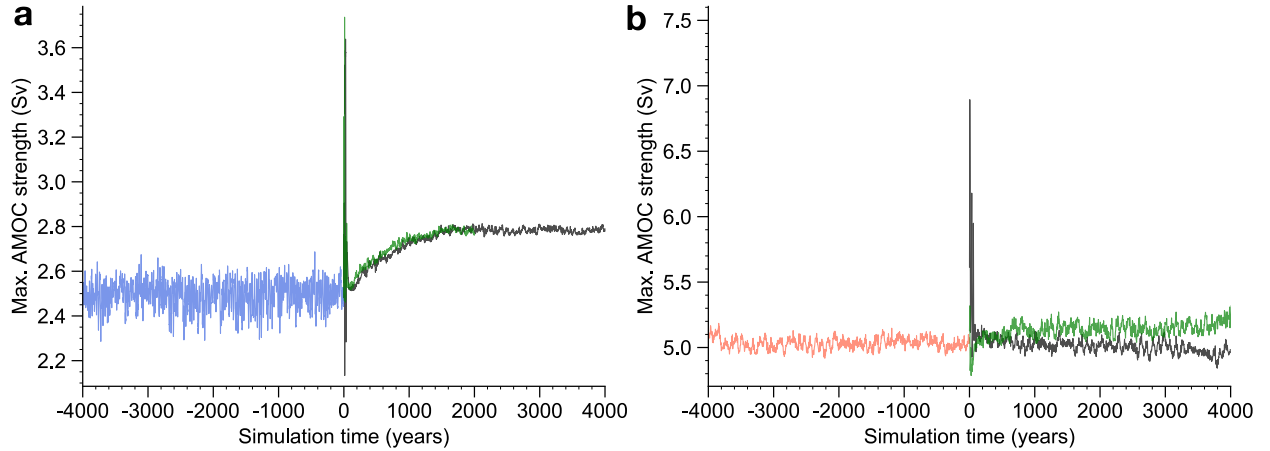


FIG. S12. **a** NH/equatorial volcanic cooling simulations initialized from a spinup simulation (blue) in the collapsed AMOC branch at $F = 0.343$, which is further away from the tipping point compared to the simulations reported in the main text (and Fig. S10), where a AMOC resurgence is triggered. Shown is a simulation with the meridional cooling profile from Fig. 6c (black), as well as a simulation where the amount of this cooling is doubled (green). Note that while no resurgence of the AMOC is triggered, there is a transition to a slightly different state, both in terms of the mean AMOC strength and its variability. This indicates further multistability beyond what is reported in Fig. S8 and Fig. 6a. **b** Volcanic cooling simulations initialized from a spinup simulation (red) at $F = 0.360$, where the AMOC is partly collapsed. No full collapse of the AMOC is induced for either a NH/equatorial (black) or SH (green) eruption scenario. However, there is a slight change in the mean AMOC, which could be a result of a transition to a slightly different stable state, and thus indicate further multistability.